Letters

A Dual-Function Planar Magnetically Coupled Current Sensor for High-Frequency Oscillation Suppression and Switching Current Measurement

Xiaokang Zhang, *Student Member, IEEE*, Qiao Li, *Member, IEEE*, Yun Huang, *Student Member, IEEE*, Guiheng Liu, *Student Member, IEEE*, and Chao Yuan, *Member, IEEE*

***Abstract*—This letter proposes a planar magnetically coupled current sensor with dual functionality: suppression of high-frequency switching oscillations and accurate switching current measurement. The sensor integrates a planar coil-based snubber circuit with a resonant compensation integrator. Through magnetic coupling, the snubber enhances power loop impedance and effectively attenuates high-frequency oscillations. Meanwhile, the resonant integrator compensates for the snubber-induced resonance, enabling precise current reconstruction. The coupled coils are embedded within the printed circuit board to achieve strong mutual inductance, supporting both effective oscillation suppression and high-sensitivity current sensing. Experimental results from a double-pulse test platform verify the sensor's dual functionality and practical applicability.**

***Index Terms*—Current sensor, planar magnetic coupling, switching oscillations.**

I. Introduction

As POWER electronic devices continue to advance, the trend toward faster switching speeds has become increasingly prevalent, driven by the demand for enhanced efficiency and higher power density. While these advancements offer significant improvements in performance, they also introduce new challenges. The elevated switching speeds lead to pronounced switching transients and oscillations, which not only contribute to additional power losses but also exacerbate electromagnetic interference (EMI), undermining overall system stability [1]. Furthermore, the precise measurement of switching currents at nanosecond timescales has emerged as a critical challenge for current sensing technologies, complicating essential tasks such as short-circuit protection and performance monitoring.

Various methods have been investigated to mitigate the adverse effects of switching oscillations, including optimizing printed circuit board (PCB) layouts to reduce parasitic inductance [2], employing active gate drivers for independent control of overshoot and oscillations [3], and incorporating snubber circuits to suppress switching oscillations [4]. Among these, snubber circuits offer a relatively simple and cost-effective solution. Compared with direct integration into the power loop, magnetically coupled snubbers avoid the risk of short circuits [5]. However, their suppression performance is limited due to weak magnetic coupling and insufficient flux linkage.

Rogowski coil current sensors (RCCS) are well-suited for high-bandwidth applications due to their wide frequency response and minimal intrusion [6]. Recent PCB-based RCCS research has focused on improving accuracy and bandwidth. For instance, Xin et al. [7] proposed a closed-loop error compensation method to precisely correct integration errors, while Li et al. [8] introduced a characteristic shaper to extend bandwidth without sacrificing sensitivity. In comparison, planar coils offer a larger effective magnetic flux area and lower parasitic parameters, making them particularly advantageous for current sensing. Furthermore, when integrated into magnetically coupled snubber circuits, planar coils enable more effective suppression of switching oscillations.

Traditionally, switching oscillation suppression and current measurement have been addressed using separate components, leading to increased system complexity and layout constraints. This letter introduces a novel dual-function planar magnetically coupled current sensor that unifies these two functions within a single, compact structure. By enabling functional reuse of the planar magnetic element, the proposed approach significantly simplifies system design while maintaining high performance in both oscillation suppression and current sensing. The sensor's dual functionality and practical effectiveness have been validated through experiments on a double-pulse test platform.

II. Principle and Design of the Proposed Planar Magnetically Coupled Current Sensor

The overall architecture of the proposed dual-function planar magnetically coupled current sensor is illustrated in Fig. 1. The sensor consists of two functional sections: Part A is a snubber circuit composed of a planar coil and a passive *RC* network, while Part B includes a voltage divider and a resonant

Received 5 May 2025; revised 7 June 2025 and 11 July 2025; accepted 6 August 2025. Date of publication 11 August 2025; date of current version 22 October 2025. This letter was supported by the National Natural Science Foundation of China under Grant U24B20102. *(Corresponding author: Qiao Li.)*

The authors are with the College of Electrical and Information Engineering, Hunan University, Changsha 410082, China (e-mail: s2209w0875@hnu.edu.cn; qiaoli@hnu.edu.cn; huangyun@hnu.edu.cn; guihengliu@hnu.edu.cn; yc2300@hnu.edu.cn).

Color versions of one or more figures in this article are available at https://doi.org/10.1109/TPEL.2025.3597418.

Digital Object Identifier 10.1109/TPEL.2025.3597418

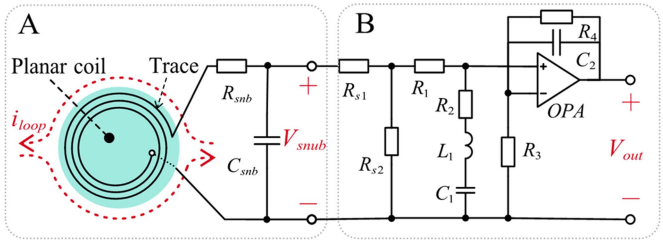

Fig. 1. Overall architecture of the dual-function planar magnetically coupled current sensor.

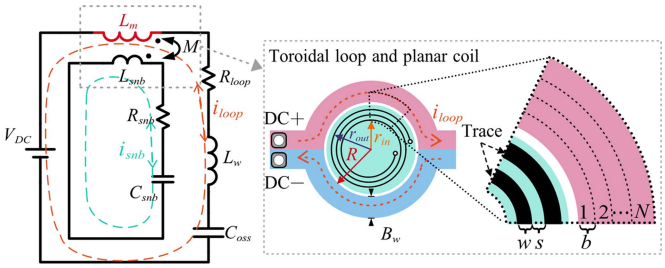

Fig. 2. Equivalent circuit of power loop with snubber circuit.

compensation integrator. The operating principle and detailed design of the sensor are presented in the following section.

A. Toroidal Loop Structure for Enhanced Mutual Inductance

The typical equivalent circuit of the power loop with snubber circuit is illustrated in Fig. 2, where L_{loop} and R_{loop} are the parasitic inductance and resistance of the power circuit, respectively, and C_{oss} is the output capacitance of the SiC MOSFET. For the snubber circuit, L_{snb} is the self-inductance of planar coil, and R_{snb} and C_{snb} are the resistance and capacitance of passive circuit.

The mutual inductance M between the power circuit and the snubber circuit is a critical design parameter, as it reflects the level of magnetic coupling. A higher M enhances both the suppression of high-frequency oscillations and the sensitivity of current sensing. To achieve strong coupling, the power loop is flexibly configured as a single-turn toroidal structure with a width B_w, as illustrated in Fig. 2. The parasitic inductance of the toroidal loop is L_m. The power loop inductance uncoupled to the planar coil is L_w. This configuration intensifies the magnetic field within the central circular region enclosed by the toroid. By placing the planar coil within this region, effective magnetic coupling with the toroidal loop can be realized. According to Faraday's law, mutual inductance can be calculated as follows:

$$M = \frac{d\phi}{di}. \tag{1}$$

For accurate computation of mutual inductance, the toroidal conductor is conceptually divided into multiple concentric current loops, each with a width b, as shown in Fig. 2. The total mutual inductance M is then obtained by summing the mutual inductance contributions from each of these concentric loops to the planar coil, as expressed by

$$\phi_{i,j} = B(r)\,S = \int_0^{r_j} \frac{\mu_0 \pi i_{\text{loop}} r_j \left(4R_i^2 - r_j^2\right)}{4NR_i\left(R_i^2 - r_j^2\right)} dr \tag{2}$$

$$M = \sum_{i=1}^{N}\sum_{j=1}^{n} \frac{d\phi_{i,j}}{di_{\text{loop}}} = \sum_{i=1}^{N}\sum_{j=1}^{n} \frac{\mu_0\pi\left[r_j^2 - 3R_i^2 \ln\left(\frac{R_i^2 - r_j^2}{R_i^2}\right)\right]}{8NR_i} \tag{3}$$

$$\begin{cases} R_i = R + b(i-1) \\ r_j = r_{\text{out}} - (w+s)(j-1) \\ N = b/B_w \end{cases} \tag{4}$$

where μ_0 denotes the vacuum permeability, R is the inner radius of the toroidal coil, n is the turns of the planar coil, r_{out} represents the outer radius of the planar coil, and w and s are the trace width and spacing of the planar coil, respectively. Another important parameter of planar coils is self-inductance L_{snb}. The simple accurate expressions of planar spiral inductors have been well established in [9]. The self-inductance for an n-turn planar coil is defined as

$$L_{\text{snb}} = \frac{\mu_0 n^2 r_{\text{avg}}}{2}\left[\ln\left(\frac{2.46}{p_r} + 0.2p_r^2\right)\right]. \tag{5}$$

The r_{avg} and fill ratio p_r are defined as follows:

$$r_{\text{avg}} = \frac{r_{\text{out}} + r_{\text{in}}}{2} \text{and} p_r = \frac{r_{\text{out}} - r_{\text{in}}}{r_{\text{out}} + r_{\text{in}}}. \tag{6}$$

The geometric parameters of the toroidal loop and planar coil are summarized in Table I, where t is the thickness of PCB copper. To validate the mutual inductance calculation method, a finite element (FEM) simulation is conducted in Ansys Maxwell using a simplified equivalent model that replicates the geometric parameters of the toroidal loop and planar coil in the actual circuit, as shown in Fig. 3. The mutual inductance calculated by FEM is 213 nH, while the analytical method gives 230 nH, resulting in a deviation of 8%. The accuracy of the mutual inductance calculation method is verified.

TABLE I
GEOMETRIC PARAMETERS

Item	Value	Item	Value
R	16.75 mm	s	0.126 mm
r_{out}	15 mm	t	1oz
r_{in}	13 mm	b	0.02 mm
w	0.126 mm	B_w	4.5 mm

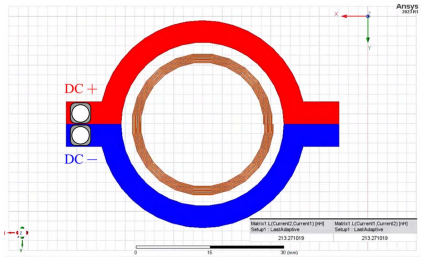

Fig. 3. FEM simulation.

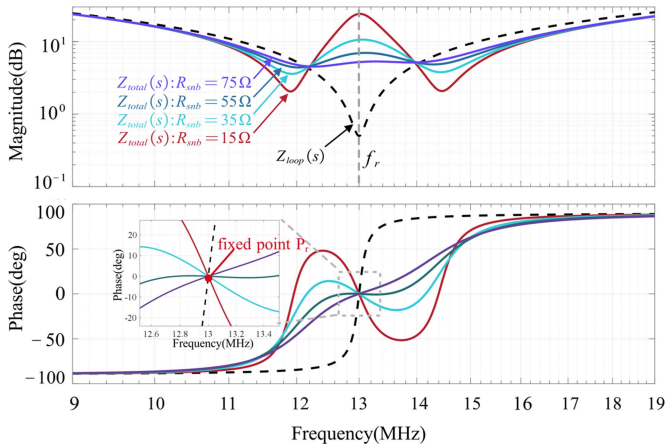

Fig. 4. Bode diagram of $Z_{\text{loop}}(s)$ and $Z_{\text{total}}(s)$.

B. Snubber Circuit Optimization for Oscillation Suppression

During switching transients, oscillations are primarily caused by the resonance between the C_{oss} and the L_{loop}. As described in [5], if the impedance of the snubber network is inserted into the power loop, the total equivalent impedance Z_{total} of the system can be expressed as follows:

$$\begin{aligned} Z_{\text{total}}(s) &= Z_{\text{loop}} + Z_{\text{snubber}} \\ &= L_{\text{loop}}s + \frac{1}{C_{oss}s} + R_{\text{loop}} + \frac{-M^2 C_{\text{snb}} s^3}{L_{\text{snb}}C_{\text{snb}}s^2 + R_{\text{snb}}C_{\text{snb}}s + 1}. \end{aligned} \tag{7}$$

The bode diagram of $Z_{\text{loop}}(s)$ and $Z_{\text{total}}(s)$ is presented in Fig. 4. It can be clearly seen that the impedance of Z_{loop} reaches its minimum value at the resonant frequency f_r. By incorporating the snubber, the impedance of $Z_{\text{loop}}(s)$ at f_r can be intentionally increased, thereby suppressing the switching oscillations. To achieve this, the resonant frequency of the snubber circuit must be designed to match that of the power loop, i.e., $L_{\text{loop}}C_{oss} = L_{\text{snb}}C_{\text{snb}}$.

The impact of different values of R_{snb} on Z_{total} is illustrated in Fig. 4. As R_{snb} decreases, the impedance of Z_{total} at the resonant frequency f_r increases. However, this also introduces two additional resonant peaks on either side of f_r, which is undesirable in practical applications. Therefore, careful selection of R_{snb} is necessary to avoid this phenomenon. From the phase–frequency characteristics in Fig. 4, it can be observed that all Z_{total} curves intersect at a fixed point P_r, regardless of the value of R_{snb}. This behavior can also be analytically derived from (5), assuming $L_{\text{loop}}C_{oss} = L_{\text{snb}}C_{\text{snb}}$. As R_{snb} increases, the slope of the Z_{total} curve around f_r transitions from negative to positive, and the impedance at f_r decreases. To maximize the impedance at f_r while avoiding the emergence of additional resonant peaks, the value of R_{snb} should be selected as follows:

$$\frac{d\left[\angle Z_{\text{total}}(j\omega)\right]}{d\omega}\Big|_{\omega=2\pi f_r} = 0. \tag{8}$$

In practical snubber circuit design, the outer radius r_{out} and number of turns n of the planar coil are first selected, as they determine the mutual inductance M and L_{snb}. Based on the resonance condition $L_{\text{loop}}C_{oss} = L_{\text{snb}}C_{\text{snb}}$ and (8), the values of C_{snb} and R_{snb} are then calculated. An enumeration method is employed to sweep r_{out} and n in order to maximize the impedance Z_{total} at the resonant frequency f_r. In Fig. 5, the results show that increasing r_{out} yields a more significant improvement in impedance than increasing n. Although both M and L_{snb} increase with the number of turns, the associated rise in L_{snb} offsets the benefits of a larger M. While a higher M improves sensing sensitivity, it also complicates circuit design. Taking these tradeoffs into account, a planar coil with $r_{\text{out}} = 15$ mm and $n = 8$ is chosen for the subsequent experiments.

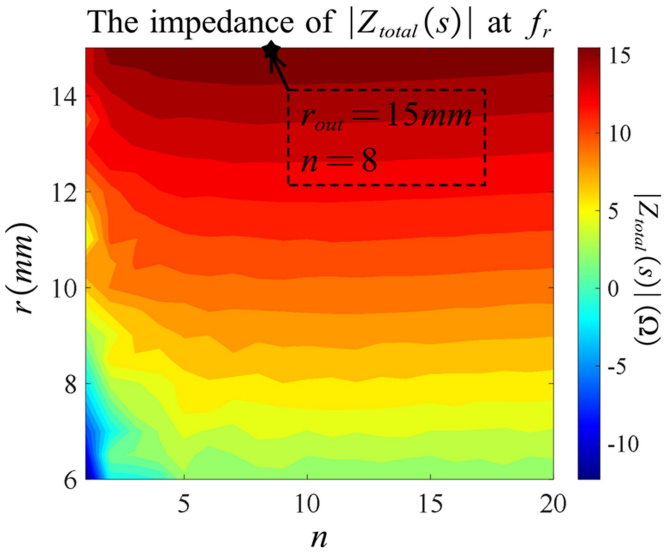

Fig. 5. Impedance of $Z_{\text{total}}(s)$ at f_r.

C. Resonant Compensation for Accurate Current Sensing

As shown in Fig. 1, to ensure the input voltage of the operational amplifier remains within its safe operating range, a resistive voltage divider composed of R_{s1} and R_{s2} is inserted between the resonant compensation integrator and the snubber. To avoid degrading the oscillation suppression capability of the snubber, R_{s1} and R_{s2} should be chosen with relatively high resistance values (on the order of kilo-ohms). Based on the equivalent circuit in Fig. 1, the transfer function of Part A, Part B, and the current sensor can be derived as follows:

$$\begin{cases} \frac{V_{\text{snub}}(s)}{i_{\text{loop}}(s)} = \frac{sMR_s}{s^2 L_{\text{snb}}C_{\text{snb}}R_{\text{snb}} + s(L_{\text{snb}} + C_{\text{snb}}R_{\text{snb}}R_s) + (R_{\text{snb}} + R_s)} \\ \frac{V_{\text{out}}(s)}{V_{\text{snub}}(s)} = \frac{R_4 R_{s2}\left(s^2 L_1 C_1 + sR_2 C_1 + 1\right)(sR_3 C_2 + 1)}{R_3(s^2 L_1 C_1 R_s + sC_1 R_s(R_1 + R_2) + sR_{s1}R_{s2}C_1 + R_s)(sR_4 C_2 + 1)} \end{cases} \tag{9}$$

$$G_{Sen}(s) = \frac{V_{\text{snub}}(s)}{i_{\text{loop}}(s)} \frac{V_{\text{out}}(s)}{V_{\text{snub}}(s)} = \frac{V_{\text{out}}(s)}{i_{\text{loop}}(s)}. \tag{10}$$

Based on (9) and (10), the frequency response of the current sensor is depicted in Fig. 6, where f_A and f_B are the resonant frequencies of Parts A and B, and ζ_{A} and ζ_{B} are the damping ratios of Parts A and B. In Part A, a pronounced resonance peak appears due to the interaction between L_{snb} and C_{snb}, which significantly restricts the sensor's bandwidth. To overcome this limitation and

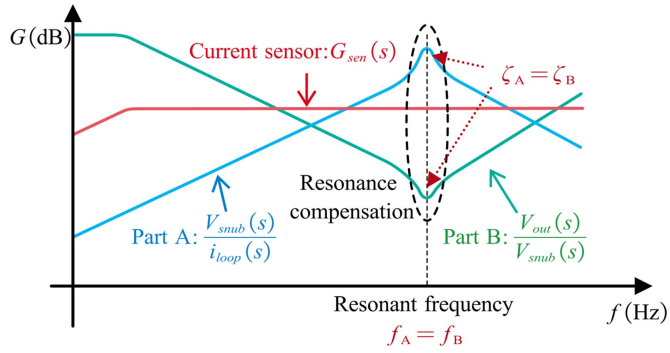

Fig. 6. Frequency responses of planar magnetically coupled current sensor.

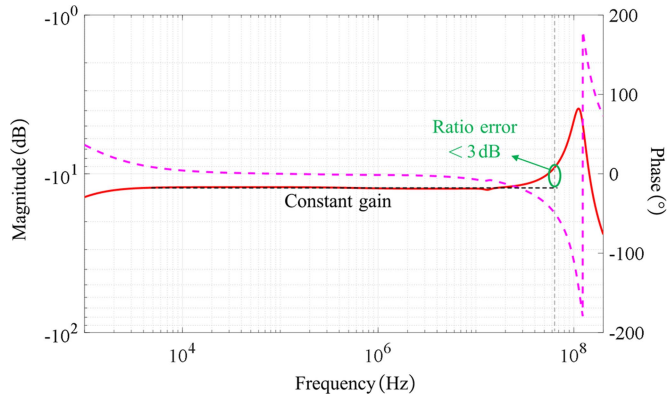

Fig. 7. Frequency responses of the current sensor.

ensure accurate measurement of high-speed switching currents, a resonant compensation integrator is implemented in Part B to extend the effective bandwidth. To compensate for the resonant peak of Part A, R_2, L_1, and C_1 are adjusted to satisfy $f_A = f_B$ and $\zeta_A = \zeta_B$. As shown in Fig. 6, Part B introduces an attenuation notch at the resonant frequency, effectively suppressing the resonance peak observed in Part A. Consequently, the overall transfer function $G_{sen}(s)$ exhibits a flatter gain response over a wider frequency range, thereby improving the sensor's accuracy in capturing fast switching current waveforms.

D. LTspice Simulation for Bandwidth Evaluation

An accurate LTspice model of the current sensor is developed to estimate its bandwidth. The impedance of the sensor circuit is accurately extracted by an impedance analyzer (WK6500B). The official Pspice model of operational amplifier LM6172 with a bandwidth of 80 MHz is applied in this simulation [10]. The frequency sweep is conducted to obtain the sensor's frequency responses, as shown in Fig. 7. It can be clearly seen that the bandwidth of this current sensor is approximately 60 MHz.

III. Experimental Verification

The prototype of the proposed current sensor and the dual-pulse test platform are shown in Fig. 8, with key system parameters summarized in Table II. Based on (9) and (10), the sensor sensitivity is calculated to be 0.24 V/A. As illustrated in Fig. 8(a), the snubber circuit is connected to the subsequent circuitry via an

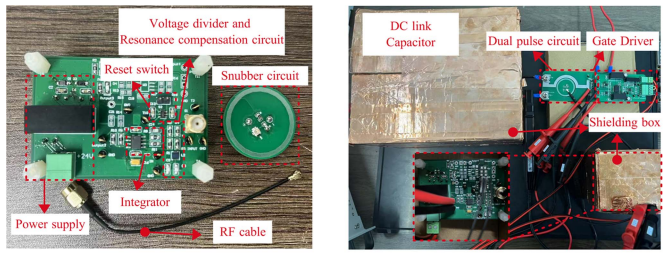

(a) (b)

Fig. 8. (a) Planar magnetically coupled current sensor. (b) Dual pulse testing platform.

TABLE II
System Parameters

Item	Value	Item	Value
L_{loop}	400 nH	R_{s2}	3 kΩ
R_{loop}	0.45 Ω	R_1	1.17 kΩ
C_{oss}	375 pF	R_2	32 Ω
M	213 nH	R_3	120 Ω
L_{snb}	3.67 µH	R_4	100 kΩ
C_{snb}	40 pF	C_1	81 pF
R_{snb}	55 Ω	C_2	2.2 nF
R_{s1}	7k Ω	L_1	1.8 µH

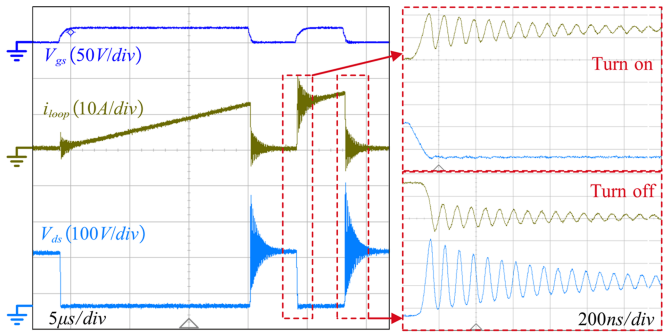

Fig. 9. Experimental results without the proposed current sensor.

RF coaxial cable. To mitigate drift errors caused by the input bias voltage and current of the operational amplifiers, a reset switch is placed in parallel with capacitor C_2 to periodically discharge the accumulated charge. Three high-bandwidth voltage probes (DP6150A, CYBERTEK) are utilized to measure the gate–source voltage, drain–source voltage, and the sensor's output voltage, respectively. For comparison purposes, the loop current is measured using a commercial current probe (HCP8030) with a bandwidth of dc–50 MHz. As shown in Fig. 8(b), to reduce EMI from the power loop and ensure measurement accuracy, the sensor circuit and voltage probes are enclosed in a shielded box.

Fig. 9 shows the double-pulse experimental results without the proposed current sensor. V_{gs} represents the gate–source voltage, i_{loop} is the loop current measured by a commercial current probe, and V_{ds} denotes the drain–source voltage of the SiC MOSFET. Significant current and voltage oscillations are observed during the switching transient, indicating severe high-frequency disturbances. In contrast, Fig. 10 presents the experimental results with the proposed current sensor, where V_{out} denotes the sensor's output voltage. It is evident that both

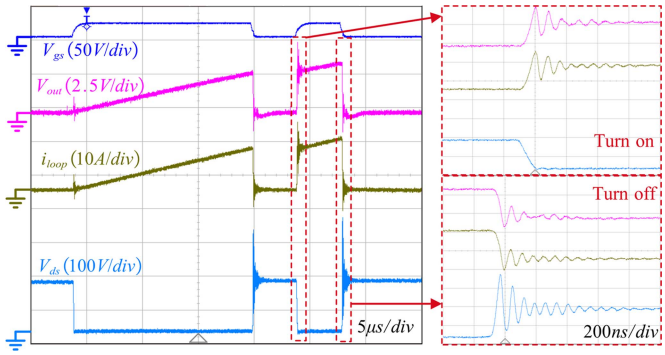

Fig. 10. Experimental results with the proposed current sensor.

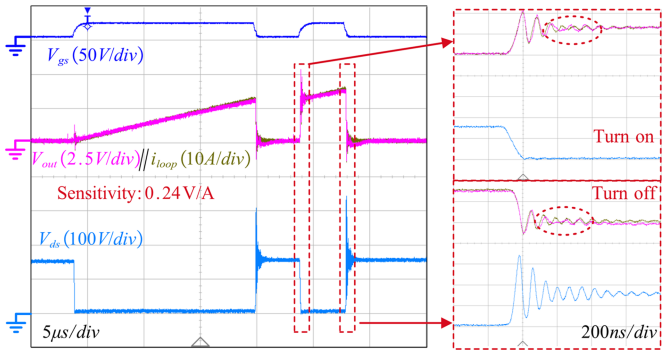

Fig. 11. Comparison between the proposed current sensor and the commercial current probe.

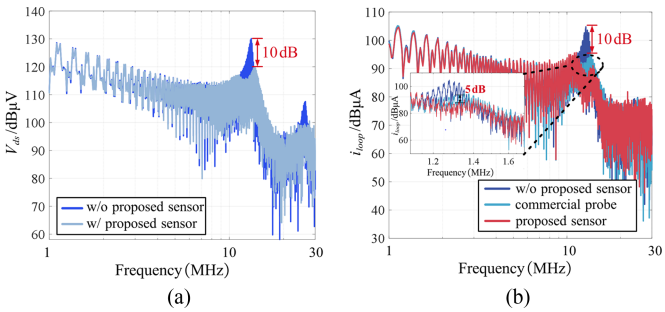

Fig. 12. Comparison of frequency spectra without and with the proposed current sensor. (a) V_{ds}. (b) i_{loop}.

current and voltage oscillations are substantially suppressed, demonstrating the sensor's effectiveness in damping switching oscillations. Furthermore, Fig. 11 overlays the switching current waveforms measured by the proposed sensor and the commercial current probe. The close agreement between the two validates the sensor's accuracy in current measurement, confirming its dual functionality of oscillation suppression and precise current sensing.

The comparison of the frequency spectra without and with the proposed current sensor is presented in Fig. 12. It is evident that the spectral peaks of both V_{ds} and i_{loop} are reduced by approximately 10 dB when the proposed current sensor is active. In Fig. 12(b), the frequency spectrum of the proposed sensor's output voltage is compared with that of a commercial current probe. Below the spectral peak, the proposed sensor exhibits a close match to the commercial probe. However, beyond the

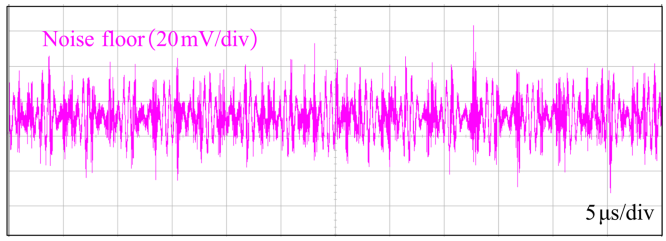

Fig. 13. Noise floor of the proposed current sensor.

TABLE III
COMPARISON WITH ADVANCE MAGNETICALLY COUPLED SNUBBER

Ref.	The reduce of spectral peaks	Magnetic core	Number of coils
Kim *et al.* [5]	6.74 dB	without	2
Li *et al.* [12]	21 dB	with	2
Liu *et al.* [13]	18.4 dB	with	2
This work	10 dB	without	1

spectral peak, the resonant-compensated integrator fails to fully compensate for the snubber-induced resonance due to nonideal circuit characteristics, leading to a deviation between the two spectra. As shown in Fig. 12(b), due to the imperfect resonance compensation. a 5 dB amplitude difference is observed near the resonant frequency. However, as shown in Fig. 11, the impact of this deviation is limited to the trailing edges of the oscillation waveform and does not significantly affect the measurement accuracy of the switching current.

The signal-to-noise ratio (SNR) of the proposed sensor is defined as the ratio of the effective signal power to the noise floor power, as expressed by

$$\text{SNR} = 10\log_{10}\left(\frac{P_s}{P_n}\right) \tag{11}$$

where P_s is the average power of the effective signal and P_n is the average power of the noise floor. With zero input, the noise floor of the proposed current sensor can be measured by a high-precision voltage probe, as shown in Fig. 13. Based on the output voltage and noise floor of the proposed current sensor, the SNR is calculated to be 40.2 dB, validating the sensor's capability for high-speed current measurement.

Table III illustrates a comparison between the proposed dual-function current sensor and several advanced magnetically coupled snubbers [5], [12], [13]. The proposed sensor achieves a greater attenuation of spectral peaks compared with [5], which benefits from the large magnetic flux area of the planar coil. Although the magnetic-core-based snubbers presented in [12] and [13] offer stronger magnetic coupling and improved oscillation suppression, they inherently increase the parasitic inductance of the power loop, which leads to more pronounced voltage overshoot. In addition, Kim et al. [5], [12], and [13] require the use of two separate coils to enhance oscillation suppression, which inevitably increases complexity and cost. In contrast, the proposed sensor achieves superior switching oscillations suppression using a single planar coil without a magnetic core, while avoiding any impact on parasitic parameters of the power loop. Therefore, it strikes a favorable balance between suppression

TABLE IV
COMPARISON WITH ADVANCED RCCS

Ref.	Rogowski coil Resonant frequency	Sensor Bandwidth	Sensitivity	Mutual inductance	Functional integration
Zhou *et al.* [7]	13.8 MHz	13.8 MHz (THS4031, 100 MHz)	100 mV/A	11.3 nH	No
Xin *et al.* [8]	42 MHz	34 MHz (THS4032, 100 MHz)	100 mV/A	9.3 nH	No
Spieler *et al.* [11]	283 MHz	185 MHz (/)	54.3 mV/A	1.08 nH	No
This work	97.1 MHz	60 MHz (LM6172, 80 MHz)	240 mV/A	213.3 nH	Yes

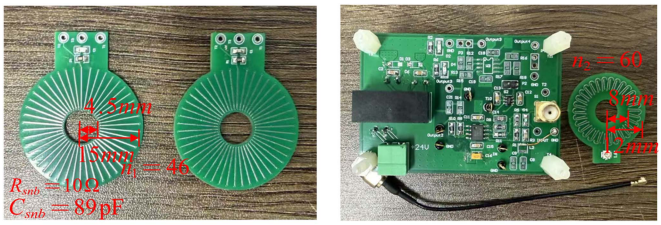

Fig. 14. (a) Discrete snubber [5]. (b) Discrete current sensor [14].

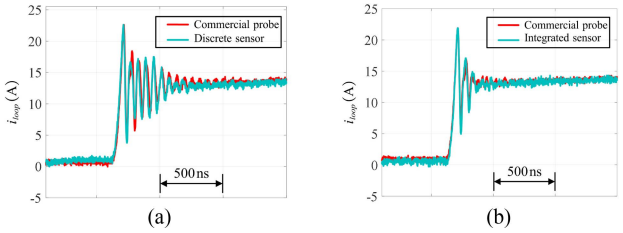

Fig. 15. Comparison between the designed current sensors and the commercial current probe. (a) Discrete sensor. (b) Integrated sensor.

effectiveness, layout simplicity, and cost-efficiency. Table IV presents a comparative performance analysis between the proposed sensor and other advanced current sensors. Benefiting from the large magnetic flux area and minimized stray parameters of the planar coil, the proposed sensor simultaneously achieves both high bandwidth and high sensitivity.

As shown in Fig. 14, an optimized discrete solution, consisting of the discrete snubbers and a discrete current sensor, is developed based on [5] and [14]. This discrete solution is compared with the proposed dual-function planar magnetically coupled current sensor to further demonstrate the advantages of the proposed integrated solution in system simplification and performance improvement. Both solutions are implemented on the double-pulse test platform, and experimental results are presented in Figs. 15 and 16. The results demonstrate that both solutions can accurately measure high-frequency switching currents and suppress switching oscillations. Specifically, the discrete solution reduces the V_{ds} oscillation duration to 76.6% and the i_{loop} oscillation duration to 84.6%. In contrast, the proposed integrated solution achieves much stronger suppression, reducing the V_{ds} oscillation duration to 15.3% and the i_{loop} oscillation duration to 30.8%. Moreover, the discrete solution requires three coils, whereas the integrated solution uses only

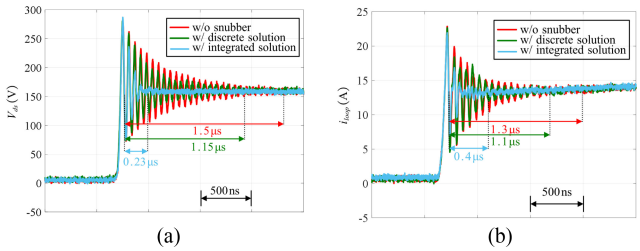

Fig. 16. Comparison of experimental results without, with discrete solution, and with integrated solution. (a) V_{ds}. (b) i_{loop}.

one. To summarize, the proposed integrated solution significantly reduces the number of components, simplifies the system, and lowers cost, while achieving stronger oscillation suppression and a better tradeoff between sensitivity and bandwidth.

IV. CONCLUSION

This letter proposes a novel dual-function planar magnetically coupled current sensor. To increase mutual inductance, the planar coil is positioned within a single-turn toroidal loop formed by the positive and negative busbars. Optimal snubber parameters are subsequently determined to maximize the impedance of the power loop at the resonant frequency. Furthermore, a resonant compensation integrator is employed to broaden the sensor's bandwidth by compensating for the snubber's resonance. Experimental results demonstrate that the proposed sensor effectively suppresses oscillations while accurately measuring the switching current. The feasibility and dual functionality of the proposed sensor have been comprehensively validated.

REFERENCES

[1] C.-W. Chang and D. Dong, "Enhanced DI/DT-RC sensing structure for accurate dynamic current measurement in paralleled SiC MOSFETs," *IEEE Trans. Power Electron.*, vol. 40, no. 7, pp. 9492–9506, Jul. 2025.
[2] H. Kong, L. Jia, L. Wang, Y. Yao, F. Yang, and H. Cui, "A flexible-PCB on DPC GaN power module with ultralow parasitic inductance," *IEEE Trans. Power Electron.*, vol. 40, no. 4, pp. 5241–5251, Apr. 2025.
[3] Q. Li, Y. Yang, Y. Wen, G. Zhang, and W. Xing, "Active gate driver with the independent suppression of overshoot and oscillation for SiC MOSFET modules," *IEEE Trans. Ind. Electron.*, vol. 72, no. 3, pp. 2325–2335, Mar. 2025.
[4] M. Xu, X. Yang, and J. Li, "C-RC snubber optimization design for improving switching characteristics of SiC MOSFET," *IEEE Trans. Power Electron.*, vol. 37, no. 10, pp. 12005–12016, Oct. 2022.
[5] J. Kim, D. Shin, and S.-K. Sul, "A damping scheme for switching ringing of full SiC MOSFET by air core PCB circuit," *IEEE Trans. Power Electron.*, vol. 33, no. 6, pp. 4605–4615, Jun. 2018.

[6] Z. Zhou, Z. Xin, Q. Liu, and C. Li, "A differential compensated air coil current sensor for switching current measurement of power devices," *IEEE Trans. Ind. Electron.*, vol. 70, no. 5, pp. 5356–5364, May 2023.

[7] Z. Xin, Y. Yao, J. Kang, Q. Li, Z. Zhou, and Y. Shi, "A closed-loop compensated Rogowski coil current sensor for three-phase inverter," *IEEE Trans. Power Electron.*, vol. 40, no. 1, pp. 2126–2138, Jan. 2025.

[8] H. Li, Z. Xin, X. Li, J. Chen, P. C. Loh, and F. Blaabjerg, "Extended wide-bandwidth rogowski current sensor with PCB coil and electronic characteristic shaper," *IEEE Trans. Power Electron.*, vol. 36, no. 1, pp. 29–33, Jan. 2021.

[9] S. S. Mohan, M. del Mar Hershenson, S. P. Boyd, and T. H. Lee, "Simple accurate expressions for planar spiral inductances," *IEEE J. Solid-State Circuits*, vol. 34, no. 10, pp. 1419–1424, Oct. 1999.

[10] LM6172 Pspice Model. [Online]. Available: https://www.ti.com.cn/product/cn/LM6172

[11] M. Spieler, C.-W. Chang, A. M. El-Refaie, D. Dong, and R. Burgos, "Design of a high-bandwidth compact DC-bus embedded planar Rogowski coil for SiC MOSFET current sensing," *IEEE Trans. Power Electron.*, vol. 39, no. 12, pp. 16482–16497, Dec. 2024.

[12] J. Li, X. Yang, M. Xu, Y. Ding, L. Wang, and J. Wang, "Investigation on optimal switching oscillation suppression for SiC MOSFET by inductively coupled damping," *IEEE J. Emerg. Sel. Topics Power Electron.*, vol. 11, no. 1, pp. 667–678, Feb. 2023.

[13] Y. Liu, X. Yang, and X. Wang, "A compact inductively coupled SiC MOSFET snubber for quasi-zero-voltage turn-on, switching oscillation, and voltage spike suppression," *IEEE J. Emerg. Sel. Topics Power Electron.*, vol. 12, no. 3, pp. 3135–3145, Jun. 2024.

[14] J. Gong et al., "Overcurrent protection enabled by broadband Rogowski coil current sensor for medium-voltage SiC MOSFET," *IEEE Trans. Power Electron.*, vol. 40, no. 5, pp. 6847–6859, May 2025.